10.21611/qirt.2023.16

Comparative Assessment of the Size-of-Source Effect in Middle- and Long-Wavelength Infrared Cameras

by M. Mendez*, J. Ebert*, L. Sommerlade*, R. Schmoll*, A. Kroll*

* *Department of Measurement and Control, University of Kassel, 34125 Kassel, Germany*

Abstract

Current radiometric calibration procedures for thermal imaging cameras are usually performed for a single calibration geometry. The uncertainty estimated from such a procedure only represents the calibration scenario and does not account for variation of the emitting source's size; this is known as the *size-of-source effect* (SSE). In this work, the measurements of the SSE for four thermal imaging cameras (two in the long-wavelength and two in the middle-wavelength infrared range) are presented. The investigation shows that the SSE rises as the temperature increase, as the size of the object deviates from the calibration geometry, and that is smaller for the middle-wavelength cameras.

1. Introduction

Similarly to pyrometers, thermal cameras are subject to the *size-of-source effect* (SSE), which is the deviation of the indicated temperature value due to the change of the measured object's dimensions [1]. If the emissivity is known, this systematic error is considered to be potentially one of the greatest contributions to the temperature measurement uncertainty [2].

Although this deviation is widely acknowledged, there are currently few sources in the literature describing it. In [3] the SSE was measured for an optical arrangement subject to a radiation source. The authors found that the SSE is associated with the scattering in the optic and internal reflections in the assembly of the optics, and suggested alternatives to reduce the occurrence of it. In [2] and [4] the modulation transfer function (MTF) of the thermal imaging system is used to describe main parts of the SSE for uncooled detector cameras. According to [2], the deviation from the theoretical behavior indicates that lower MTF values entail a contrast reduction, which leads to the SSE. However, [4] point out that a single MTF measurement cannot fully describe all the root causes involved, such as crosstalk of sensor elements and residual errors of nonlinearity correction, among others. Other researchers opted for a direct measurement approach. In [5], the SSE was studied for a long-wavelength infrared (LWIR) camera with different aperture geometries in front of a black body and different distances between the aperture and the camera. The authors concluded that the SSE is not negligible and should be specified by the manufacturers. In [6], the SSE was measured for two LWIR cameras and a method for its compensation was proposed, based on an image processing approach. The authors reveal that the SSE affects the uncertainty of the measurement, and the application of a digital filter was able to reduce the temperature deviations to achieve the deviations ranges specified by the manufacturer. Likewise, [7] measured the SSE of three LWIR cameras, two with microbolometer sensors and one with a cooled mercury cadmium telluride (MCT) sensor for a plate radiator at a temperature of 100 °C. The results indicate lower values of the SSE for the camera with the cooled detector.

In the present work, the SSE was measured for two LWIR and two mid-wavelength infrared (MWIR) cameras at three different black body temperatures. For both groups of cameras, the optical configuration significantly differs, see Table 1. The paper is structured as follows: Sect. 2 describes the cameras studied and the experimental setup. The results are presented and discussed in Sect. 3. Finally, Sect. 4 presents the conclusions and provides an outlook on the work planned in the near future.

2. Methodology

The SSE is caused by different reasons, as it is described in the literature. The influence of the thermal camera configuration, expressed in detector technology and optical components, and the behavior of SSE at different temperatures was evaluated through an experimental study. In this section is depicted, the experimental setup, the measurement procedure and how the SSE was assessed from the measurements.

2.1 Experimental setup

The investigations were carried out for four cameras. Each one of these operates in a different spectral measurement range (two in the LWIR and two in the MWIR), with a different optical configuration. The relevant technical information is presented in Table 1.

A Fluke 4180 infrared calibrator (plate radiator) was utilized to have a suitable surface with homogeneus and known temperatures. According to the technical specification, the infrared calibrator has a spatial uniformity of $\pm$ 0.25 °C in a

diameter of $5\,\mathrm{in}$ aligned to the center of the surface. This uniformity value is lower than the temperature deviations associated with the SSE. The calibrator is equipped with a controller that holds the temporal fluctuations of the surface temperature within a $\pm\ 0.10\,^{\circ}\mathrm{C}$ range.

Apertures of finnboard were placed in front of the calibrator (see Fig. 1) to vary the size of the observed radiator surface. This material was chosen because of its high emissivity (above 0.90), which prevents it from reflecting radiation from surrounding objects; its low thermal conductivity, which prevents it from heating up; and it is easily cutted by laser, which ensures smooth surfaces at the cut edges.

The geometric pattern preferred for the study was the circumference, since it allows obtaining symmetry in axes oriented in any direction. If a different geometry would be chosen, e.g. triangle or square, the distance from the edge of the aperture to the pixel in the middle of the observed radiation surface would vary over the perimeter of the geometrical pattern.

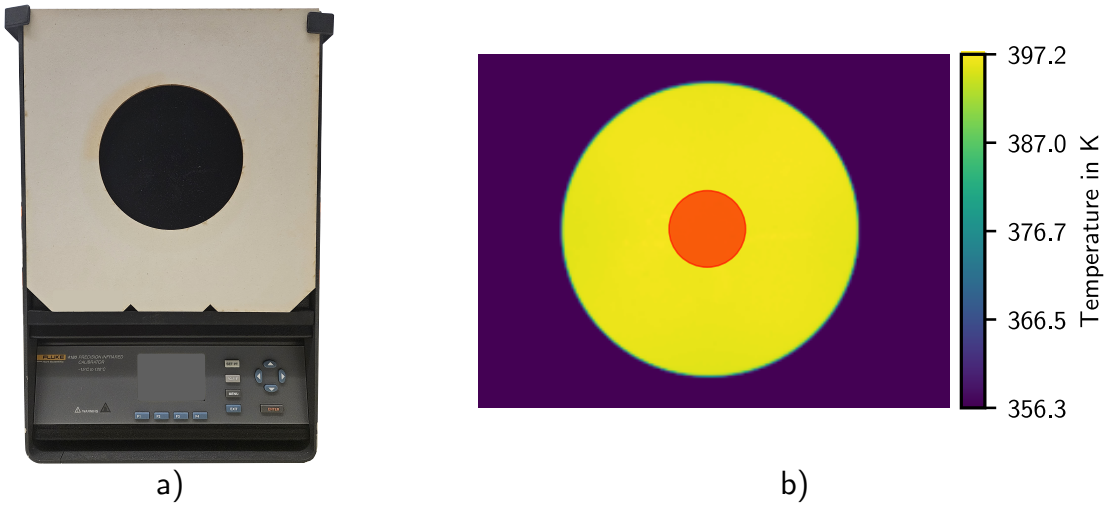

Fig. 1. *Infrared calibrator with a finnboard aperture (a), and the respective thermogram (b) obtained with the camera 3 at* T_{set} : $393.15\mathrm{K}$. *The red circle refers to the region of interest (ROI) in which the figures of merit are calculated.*

The diameters and distances considered were selected in order to obtain aperture diameters in the image in a range from at least 9 pixels up to 99 % of the image height in pixels. Table 2 lists the diameters and distances for which the measurements were made with each camera.

2.2 Data acquisition

The SSE was studied for three black body temperature set points T_{set} of the plate radiator:

$$T_{\mathrm{set}} : (323.15, 363.15, 393.15)\ \mathrm{K}$$

delimited by the operation range of the used device.

Table 1. *Technical data of the studied cameras. The specified measurement ranges are composed by subgroups which can be selected for the respective camera. On the table, UC stands for uncooled.*

Specification	Unit	Camera 1 (LWIR)	Camera 2 (LWIR)	Camera 3 (MWIR)	Camera 4 (MWIR)
Spectral range	µm	7.5 to 14	7.5 to 13	3.2 to 3.4	2.0 to 5.7
Detector format $W \times H$	px	640×480	382×288	320×240	640×512
FOV	°	30×23	62×49	24×18	5.5×4.4
f / F	mm / -	30 / 1	8 / 0.8	23 / 1.5	100 / 3.0
Measurement range	°C	-40 to 1200	-20 to 900	-40 to 350	-40 to 3000
Uncertainty	-	± 1.5 K (0 to 100)°C or 2 %	± 2 K or ± 2 %	± 1 K (0 to 100)°C or ± 2 %	± 1 K (0 to 100)°C or ± 1 %
Detector element	-	UC microbolometer	UC microbolometer	Cooled InSb	Cooled InSb

For each T_{set}, it was waited until the steady state had been reached (after 10 minutes). Next, the camera was placed in front of the infrared calibrator, and the optical center was aligned with the center of the plate radiator surface by visual inspection, since the positioning was not performed with a rigid assembly.

The aperture was placed, and the focus of the images was done on the circumference edge. Before each measurement, the cameras were shielded from the radiance emitted by the infrared calibrator, to prevent the detectors from heating up, and the non-uniformity correction (NUC) of the cameras was performed. 50 consecutive images were obtained from each measurement point, which were then averaged to reduce the temporal noise. The ambient temperature and the relative humidity were measured for monitoring the measurement conditions and for correcting the deviations associated with the transmittance of the air, specially for the camera 4 due to its measurement distance. These values, in conjunction with the emissivity of the plate radiator, were introduced in the cameras' software modules in order to perform the respective corrections. The apertures were placed from largest to smallest diameter.

During the measurements, a pyrometer was used to supervise the temporal fluctuations of the surface temperature. The instrument was placed at a distance at which a sufficiently small measurement region was projected on the calibrator surface, compared with the observed radiant surface from the smallest aperture. This procedure was performed for the entire apertures.

2.3 SSE assessment

The SSE was evaluated by means of two figures of merit. The first one is the absolute deviation of the temperature:

$$\Delta T_i = T_i - T_{\text{ref}} \tag{1}$$

where T_i refers to the mean temperature value in a region of interest (ROI) for the i-th aperture, and T_{ref} to the obtained value at the widest aperture for each camera, as it is indicated in the German technical guideline VDI/VDE 5585 Part 1 - Section 4.27 [1]. A temperature measurement with an external instrument was not contemplated, since the aim of the study was not to evaluate the calibration of the cameras but the variation of the measured temperature with the size of the radiating surface.

The second figure of merit is the relationship between the radiance values:

$$\theta_i = \frac{L_i}{L_{\text{ref}}} \tag{2}$$

where L_i and L_{ref} are the correspondent values for T_i and T_{ref}, which are calculated from the numerical integration of the plank's law:

$$L(\lambda, T) = \int_{\lambda_1}^{\lambda_2} \frac{2hc_0^2}{\lambda^5 \left(\exp\left(\frac{hc_0}{\lambda k T}\right) - 1\right)} d\lambda \tag{3}$$

where h is the Planck constant, c_0 is the speed of light in a vacuum, λ is the wavelength and k the Stefan-Boltzmann constant.

The region of interest (ROI) was defined as a concentric circular region, whose diameter corresponds to a quarter of the aperture diameter in the image, as it is also indicated in the VDI/VDE 5585 Part 1 - Section 4.27 (see Fig. 1). A second ROI with a fixed size was also chosen for calculating the variables. The difference in the results are discussed in Sect. 3. To present the results, a relative aperture diameter was used:

$$d_{\text{rel}} = \frac{d_{\text{px}}}{H} \tag{4}$$

where d_{px} refers to the diameter obtained in the image in pixel units and H the vertical resolution of the camera. The coordinates of the center and the radius of the circle were obtained by means of the digital image processing algorithm *HoughCircles* of the *OpenCV* library [8]. The data was postprocessed with self developed python scripts.

Table 2. *Distances and diameters considered for the evaluation of the SSE.*

Camera	Distance in cm	Aperture diameters in mm	Aperture diameters in px	Relative diameters in %
1	33.2	$\{20, 40, 60, 80, 100, 120\}$	$\{82, 162, 242, 320, 400, 476\}$	$\{17, 34, 50, 67, 83, 99\}$
2	18.2	$\{5, 26, 52, 83, 115, 140\}$	$\{10, 54, 106, 170, 228, 278\}$	$\{3, 19, 36, 58, 81, 96\}$
3	40.0	$\{5, 21, 52, 69, 91, 114\}$	$\{9, 38, 90, 122, 162, 198\}$	$\{3, 31, 50, 66, 83\}$
4	200.0	$\{5, 26, 52, 91, 114, 139\}$	$\{16, 88, 176, 306, 386, 468\}$	$\{4, 17, 34, 60, 75, 91\}$

3. Results and Discussion

The calculated figures of merit are presented in Fig. 2 and 3. The results are discussed around four main topics: The influence of the size of the ROI, the variation of SSE with the temperature, the compliance of SSE with respect to the reference ranges indicated for the variables evaluated, the effect of optical accessories and the MTF.

Dimension of the ROI: The figures of merit were calculated considering a radius of 3 px for the circular ROI, which results are presented in Fig. 3. This was done in order to see if a deviation arises due to a possible non-homogeneity of the surface towards the edges of the plate radiator, or the results are affected by the number of pixels considered for the calculations. As it can be seen, slightly larger ΔT values are obtained with the 3 px ROI, but no significant differences are observed from the results presented in Fig. 2, in terms of the courses of the curves and the performance of the cameras.

Relationship of the SSE with the temperature: The temperature deviations ΔT are presented on the left column in Fig. 2 and 3. For the four cameras, ΔT rises as the temperature increases. The camera 3 delivered the lowest ΔT for all the considered temperature set points and diameters. The curve of the camera 1 intersects with the curve of the camera 4, and determine two regions for which opposite behaviors occur. For the left side of the intersection point (e.g. $d_{\text{rel}} < 34$ % for $T_{\text{set}} = 323.15\,\text{K}$), the magnitude of ΔT is lower for the camera 4, compared with the camera 1, while on the right side, the magnitude of ΔT is greater, compared with the same camera. As the temperature increases, this point of intersection moves to the right, indicating that the SSE for the camera 4 is lower for a wider range of d_{rel}; for $T_{\text{set}} = 393.15\,\text{K}$, the curve of camera 4 is above the curve of camera 1. The camera 2 shows the largest ΔT for the three temperature set points.

Regarding θ, as for ΔT, the deviation is greater as the temperature increase (the values of θ deacrease for each d_{rel}) for the studied cameras. The camera 1 depicted the lowest deviations from the ideal value ($\theta = 1$) for $T_{\text{set}} = 323.15\,\text{K}$. The camera 2 and 3 exhibits a similar behavior for this temperature set point, and the greatest deviation is observed for the camera 4 for $d_{\text{rel}} > 25$ %. For $T_{\text{set}} = 363.15\,\text{K}$, θ declines the less for the camera 3, similarly for the camera 1 and 4, and the most for the camera 2. For $T_{\text{set}} = 393.15\,\text{K}$, a reduction of θ is observed for the entire curves of the cameras 1 and 2, meanwhile for the cameras 3 and 4, the reduction is mainly observed at the smallest aperture. For the cameras 1, 3 and 4, the values of θ are bounded 0.97, whereas for the camera 2, it decreases below 0.95.

From both figures of merit, it was observed the SSE is less pronounced at high temperatures for cameras with cooled detectors compared with cameras with microbolometer detectors. A dependency of the SSE with the detector technology was reported also in [7], where the lowest ΔT were observed for the camera with the cooled detector and the biggest ΔT were obtained for the cameras with the uncooled detector.

Comparison of the SSE within the uncertainty intervals specified by the manufacturers and/or in the literature: This section compares whether the variables analyzed are in line with the expected deviations, given by the cameras manufactures or suggested in the literature. As it is known, the uncertainty ranges are calculated after the calibration of the cameras, and are referenced to the measured values at the geometry used for this procedure. For the sake of comparison, the SSE should be evaluated taking as the reference this geometry, which is not known for all cameras. For this reason, the half of the absolute temperature difference ΔT is compared with the expected deviation of the measurement:

$$\frac{\Delta T}{2} < u_c \tag{5}$$

where u_c refers to the uncertainty value obtained from the indications of the manufacturer listed in Table 1. The ΔT values were halved, assuming the calibration was performed at the geometry where the SSE distributes the best for the entire range size. This would be for instance the case of the camera 2 for $T_{\text{set}} = 393.15\,\text{K}$, if this would be calibrated circular geometry with a diameter of about $d_{\text{rel}} = 40\%$. Regarding the radiance relationship $\theta = \frac{L_i}{L_{\text{ref}}}$, [9] indicated that a deviation within 2 % is acceptable:

$$\frac{1-\theta}{2} \cdot 100\ \% < 2\ \% \tag{6}$$

The compliance of the conditions specified in (5) or (6) were calculated for the four cameras and the results are presented in Table 3. The camera 2 does not meet the condition (6) for $T_{\text{set}} = 363.15\,\text{K}$, and for $T_{\text{set}} = 393.15\,\text{K}$, both conditions were not satisfied. The other cameras satisfy the conditions in all cases.

Optical accessories: With respect to the optics of the camera, the focal length f shows no clear trend. For the LWIR cameras, the lowest ΔT are obtained for the lower f (camera 1), while the opposite is true for the MWIR cameras (camera 3). The parameter F, which can be expressed as the relationship $\text{F} = \frac{f}{D}$ between the focal length f and the aperture stop D, shows also opposite tendencies for the mentioned camera groups. The biggest ΔT are observed from the camera with the largest F number in the MWIR group (camera 4), whereas the opposite is seen in the LWIR group (camera 1). Notwithstanding, for both cases, lower ΔT values are observed for F values close to 1. In [2] it was shown that, as the F number increases for an optical system, the reduction in contrast is more evident and the SSE takes place. However, this was carried out for $F \geq 1$ and not for values under 1.

A couple of details should be mentioned for the comparison of the cameras. On the one hand, the price of the LWIR cameras may influence the quality of the optical accessories and consequently the amount of scattered radiation may be lower for the camera 1 (the price of this camera is an order of magnitude above the price of the camera 2). On the other hand,

Table 3. *Obtained values of the variables ΔT and θ at the smallest aperture. The uncertainty value u_c is presented for comparison reasons. The cells marked with yellow show the cases when the analyzed figures of merit are outside the ranges indicated for the manufactures or in the literature [9].*

Variable	u_c **in K**			$0.5 \cdot \lvert\Delta T\rvert$ **in K**			$0.5 \cdot (1-\theta)$ **in %**		
T_{set}	323.15 K	363.15 K	393.15 K	323.15 K	363.15 K	393.15 K	323.15 K	363.15 K	393.15 K
Camera 1	1.5	1.5	2.33	0.43	0.90	1.30	0.59	0.99	1.24
Camera 2	2	2	2.25	0.99	1.92	2.80	1.38	2.23	2.74
Camera 3	1	1	2.44	0.27	0.35	0.51	1.12	1.05	1.39
Camera 4	1	1	1.21	0.35	0.65	0.80	1.00	1.48	1.56

for the MWIR cameras, the camera 3 was designed for a dedicated application (considering the narrow spectral band), while the camera 4 is intended for multiple purposes. This implies that more optical accessories are required on the optical path to achieve the expected quality of the measurements, which increases the scattering and consequently increases the SSE, as it was shown in [3].

MTF: The courses of the MWIR cameras' curves for the three smallest apertures is not the same for the respective ones of the LWIR cameras. For $d_{\text{rel}} = 17\%$, the progression of the curve, observed from the right to the left, is disrupted, and a pronounced decline is observed (especially for θ). This could be explained from the MTF of the camera. As the spatial frequency increase, the MTF diminishes, the reduction in contrast take place and the SSE is observed, as it was discussed in [2]. Nevertheless, the evidence is not definitive for concluding this and direct measurements addressing this have to be carried out.

4. Conclusion and Outlook

The SSE was measured and assessed for two LWIR (1 & 2) and for two MWIR cameras (3 & 4), each with a different optical configuration. The values obtained using the MWIR cameras showed overall lower deviations compared to the LWIR cameras. In both cases, the deviation increases with higher temperatures and smaller apertures. The figures of merit proposed for studying the SSE were compared with the uncertainty ranges of the cameras and the limits suggested in the literature. Since the calibration geometry of all cameras was not known, the calculated values were halved in order to assume the best geometrical distribution of the SSE. The camera 2, according to this scenario, is the only one that is outside the accuracy range, and the limits suggested for the radiance relationship by [9], for $T_{\text{set}} = 393.15\,\text{K}$. The importance of the calibration geometry was also mentioned in [10], who emphasized the importance of addressing the aperture size at which the calibration took place, when the SSE is assessed for radiation thermometers. A comparison of the optical parameters was carried out, but no definitive tendency was found. Some assumptions could be made from the F-number, but the differences in the results can arise from the quality of the lens and not the parameters themselves. A pronounced decline of the curves for $d_{\text{rel}} < 17\%$ is observed for the MWIR cameras, which is not seen for the other apertures. An association with the MTF could explain this, since the reduction in contrast occurs as the spatial frequency increases. However, the evidence is not definitive to conclude it. In that sense, more specific studies addressing the influence of the optics and the MTF have to be performed. For the future work, the study will be carried out for higher T_{set} ($T_{\text{set}} \leq 500\,^{\circ}\text{C}$), in order to address the behavior of the SSE at these temperatures, where different radiance magnitude orders take place. Moreover, the SSE will be measured for the camera 4 with different optical objectives.

5. Acknowledgments

This work is supported by the Federal Ministry for Economic Affairs and Climate Action (BMWK) on the basis of a decision by the German Bundestag.

References

[1] Verein Deutscher Ingenieure. VDI/VDE 5585 Part 1. Temperature measurement with thermographic cameras - Metrological characterization, 2018.

[2] H. Budzier and G. Gerlach. The size-of-source effect in thermography. *Journal of Sensors and Sensor Systems*, 10(2):179–184, 2021.

[3] H. Yoon, D. Allen, and R. Saunders. Methods to reduce the size-of-source effect in radiometers. *Metrologia*, 42(2):89–96, 2005.

[4] S. Schramm, J. Ebert, R. Schmoll, and A. Kroll. Compensating the size-of-source effect: Relationship between the MTF and a data-driven convolution filter approach. In *16th Quantitative InfraRed Thermography Conference (QIRT)*, 2022.

[5] I. Pušnik and G. Geršak. Evaluation of the size-of-source effect in thermal imaging cameras. *Sensors*, 21(2):1–22, 2021.

[6] S. Schramm, R. Schmoll, and A. Kroll. Compensation of the size-of-source effect of infrared cameras using image processing methods. In *13th International Conference on Sensing Technology (ICST)*, pages 1–6, 2019.

[7] S. König, B. Gutschwager, R. D. Taubert, and J. Hollandt. Metrological characterization and calibration of thermographic cameras for quantitative temperature measurement. *Journal of Sensors and Sensor Systems*, 9(2):425–442, 2020.

[8] G. Bradski. The OpenCV Library. *Dr. Dobb's Journal of Software Tools*, 2000.

[9] J. McMillan. *Traceable thermal imaging in harsh environments*. PhD thesis, University of Surrey, 2023.

[10] G. Machin and G. Sergienko. A comparative study of size of source effect SSE determination techniques. In *TEMPMEKO 01. 8th International Symposium on Temperature and Thermal Measurements in Industry and Science*, volume 1, pages 155–160, 2001.

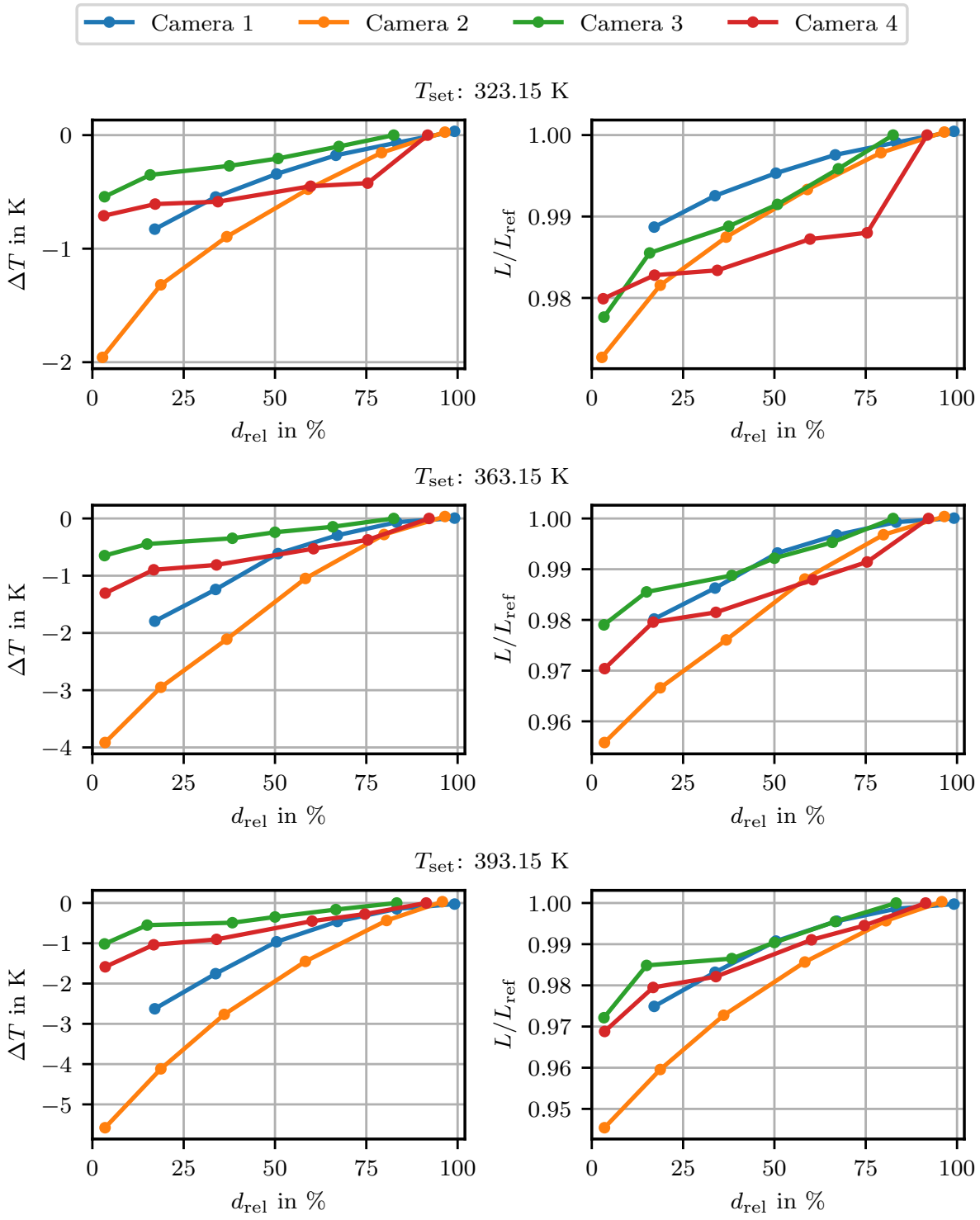

Fig. 2. *Measured figures of merit for the cameras listed in the Table 1. The radius of the circular ROI was set to one quarter of the radius of the aperture. The reference temperature was obtained from the largest opening.*

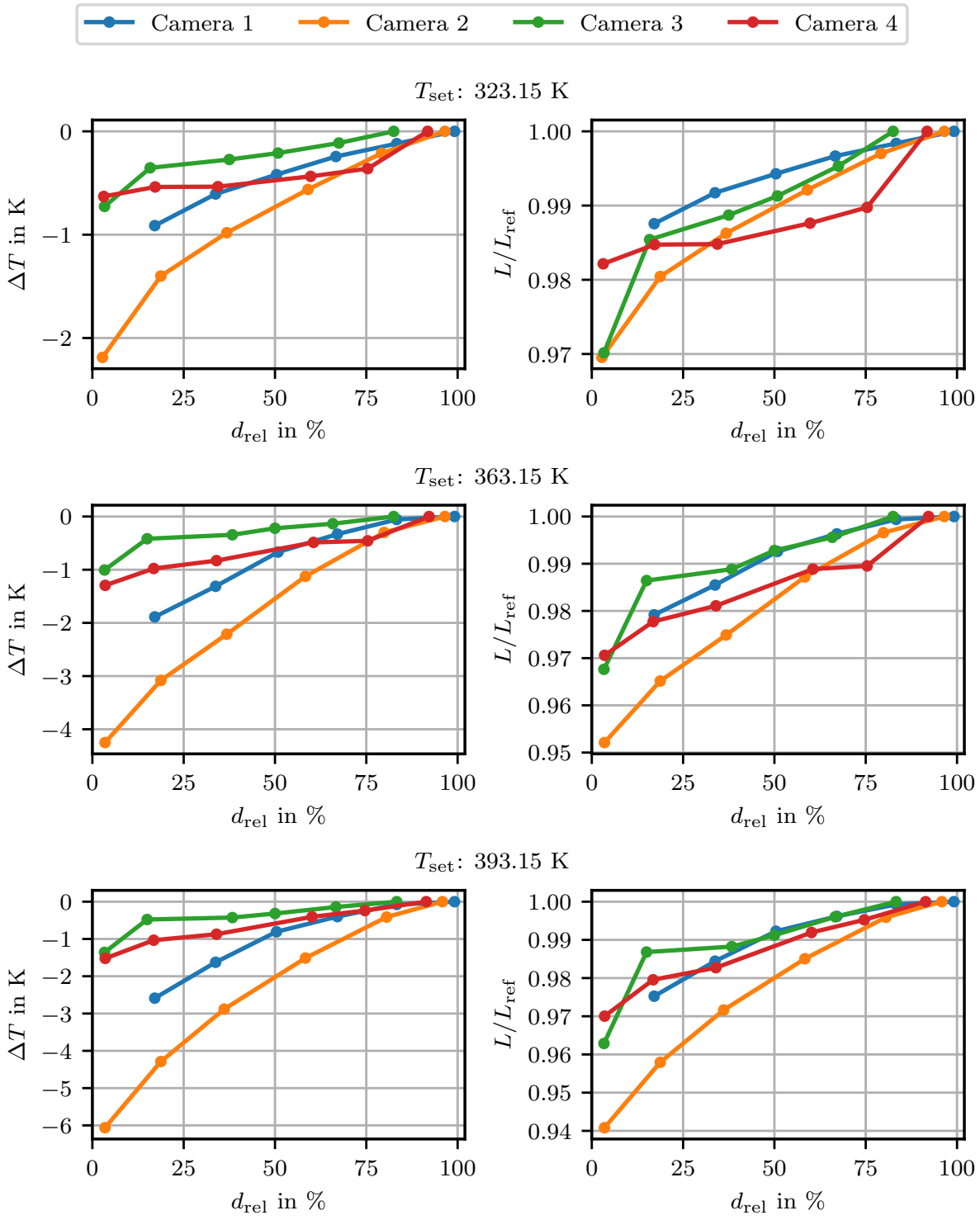

Fig. 3. *Measured figures of merit for the cameras listed in the Table 1. The radius of the circular ROI was set constant to 3 px. The reference temperature was obtained from the largest opening.*